INORGANIC CHEMISTRY
FRONTIERS

RESEARCH ARTICLE

View Article Online
View Journal | View Issue

Cite this: *Inorg. Chem. Front.*, 2018, **5**, 2211

Porous Fe–N-codoped carbon microspheres: an efficient and durable electrocatalyst for oxygen reduction reaction†

Xianghong Li, Xu Sun,* Xiang Ren, Dan Wu, Xuan Kuang, Hongmin Ma, Tao Yan and Qin Wei *

Received 23rd June 2018,
Accepted 20th July 2018

DOI: 10.1039/c8qi00592c

rsc.li/frontiers-inorganic

Electrochemical oxygen reduction is a key process for many energy storage and conversion devices, and finding highly efficient, economical, and durable electrocatalysts to replace the Pt-based catalyst for the oxygen reduction reaction (ORR) is a critical obstacle. In this article, porous Fe–N-codoped materials are obtained by pyrolysis of a defined precursor of polydopamine-coated Fe_3O_4 as not only template but also nitrogen and iron source. In 0.1 M KOH, the as-prepared catalyst exhibited high ORR activity (onset potential of 0.949 V and half-wave potential of 0.836 V *vs.* RHE), with excellent electrochemical stability, durability and remarkable tolerance toward methanol. The successful synthesis of porous nanospheres provides a novel way to explore a series of mesoporous metal electrocatalysts for energy conversion.

Introduction

In recent years, fuel cells have attracted increased attention due to the rapid depletion of traditional fossil fuels and the increased global demand for clean and renewable energy.[1,2] The oxygen reduction reaction (ORR) at the cathode has sluggish kinetics compared with the oxidation of hydrogen at the anode and is thus a bottleneck for improving the energy transfer efficiency of fuel cells.[3–5] Today, a precious metal (Pt)-based electrocatalyst is often adopted for ORR, but quantity production is restrained by its rarity and poor long-term durability.[6] Carbon-based materials have many merits such as simple process of preparation, cheap base material and abundant supply of nonprecious metals, *etc*.[7–17] Thus, great efforts have been devoted to developing carbon-based catalysts with long-term durability.

Doped carbon materials show enormous potential to replace the Pt-based catalyst in consideration of their enhanced electrocatalytic activity as well as increased electrical conductivity; these include metal- and nitrogen-codoped carbons (M–N/C),[7–12] nonmetal heteroatom/C[13–15] and MO_x–carbon composites.[16,17] Fe–N/C materials could be the most promising alternative owing to their high ORR activity.[7–12] For the synthesis of Fe–N-codoped catalysts, traditional templates such as silicon dioxide have frequently been adopted. However, the removal of these templates is time-consuming,[11] severe and harmful to the environment due to the application of strong acid.[12] In this regard, rational design of electrode materials with high performance and stability is still required for electrocatalysts.

Here in our work, novel porous Fe–N-codoped carbon microspheres (PFCMs) were successfully fabricated. This material was synthesized using glucose as the carbon support and polydopamine-coated Fe_3O_4 spheres (PDCFs) as not only the nitrogen and iron source but also the template. Our material exhibits several properties that are highly important for effective performance: (1) presence of graphitic domains bringing about enhanced electronic conductivity; (2) occurrence of a large number of nitrogen functional groups as well as iron–nitrogen coordination sites; (3) high specific surface area and porosity ensure good contact with O_2 and electrolyte. Benefiting from the above-mentioned factors, PFCMs exhibits excellent catalytic activity with high onset potential of about 0.949 V and half-wave potential of about 0.836 V *vs.* the reversible hydrogen electrode (RHE). Notably, it also shows high electrochemical stability, durability and methanol tolerance. The successful synthesis of nanospheres provides a novel way to explore a series of mesoporous metal electrocatalysts for energy conversion.

Experimental section

Materials

Materials and reagents, including ferric chloride hexahydrate (AR), dopamine hydrochloride (98%), tris(hydroxymethyl)-aminomethane (Tris, 99.8%), glucose (AR), ethylene glycol (AR),

Key Laboratory of Chemical Sensing & Analysis in Universities of Shandong, School of Chemistry and Chemical Engineering, University of Jinan, Jinan 250022, Shandong, PR China. E-mail: chm_sunx@ujn.edu.cn, sdjndxwq@163.com

†Electronic supplementary information (ESI) available: Experimental section and supplementary figures. See DOI: 10.1039/c8qi00592c

potassium hydroxide (KOH, GR), hexamethylenediamine (AR), Pt/C (20 wt%), hydrochloric acid (37% HCl), Nafion (D-520), isopropyl alcohol (AR) and sodium acetate (AR), were procured from J&K Scientific Ltd (Shanghai, PR China) and Aladdin (Shanghai, PR China). All solutions were prepared with ultrapure water (18.25 MΩ cm from an UP system).

Synthesis of PDCFs nanoparticles

Fe_3O_4 magnetic nanospheres were prepared by a hydrothermal protocol. Briefly, 5.4 g of $FeCl_3{\cdot}6H_2O$ was dissolved in 300 mL ethylene glycol, and then 14.4 g sodium acetate was added to this yellow solution. After ultrasonication several times, the resulting solution was transferred into a Teflon-lined stainless steel autoclave. The autoclave was kept at 200 °C for 14 h. After that, the black magnetic microspheres were collected with the help of a magnet, followed by washing with ethanol and deionized water five times.

Polydopamine nanospheres (PNANs) with excellent dispersibility were prepared according to a previous report.[18] Using 50 mg dopamine hydrochloride, 25 mL Tris-buffer and isopropyl alcohol (pH = 8.8), PDANS were obtained by controlling the reaction time to 24 h. Next, 50 mg Fe_3O_4, 100 mg polydopamine and 60 mg Tris were dissolved in 50 ml water, which was stirred for 30 h at room temperature. The product was collected *via* vacuum filtration.

Preparation of PFCMs microspheres

Two hundred milligrams of PDCFs was redispersed in glucose solution (0.2–0.5 M) *via* ultrasonication several times. Then the slurry was transferred to an autoclave and kept at 180 °C for 12 h. After that, the chamber was cooled to room temperature. Carbon-coated PDCFs (CPDCFs) were obtained and washed *via* vacuum filtration. CPDCFs were dried under vacuum overnight. After annealing in Ar atmosphere for about 1 h, PFCMs was successfully obtained. By varying the annealing temperature from 700 to 1000 °C, various materials were obtained, which were named PFCMs-700, PFCMs-800, PFCMs-900 and PFCMs-1000, respectively.

Catalyst characterization

The crystal structures of the synthesized materials were analyzed by X-ray diffraction (XRD) using a Bruker AXS D8-Advanced diffractometer equipped with Cu Kα radiation (λ = 1.5406 Å) operated at 40 kV and 20 mA. Structural defect level of catalysts was analyzed by Raman spectrometry (Horiba LabRAm HR Evolution spectrometer) at room temperature. The source of radiation was a laser operating at a wavelength of 532 nm. The range of the measured spectra was from 33 to 3300 cm^{-1}. X-ray photoelectron spectroscopy (XPS) was carried out on an ESCALAB 250 spectrometer (Thermo Fisher) using Al Kα radiation (h = 1253.6 eV). The quantitative analyses of Fe and N were based on the peak intensities of N 1s and Fe 2p signals, respectively. The N 1s and Fe 2p XPS spectra were obtained by least squares fitting using Gaussian–Lorentzian curves. The morphology and microstructures of as-prepared samples in each synthetic step were investigated by scanning electron microscopy (SEM; Quanta FEG 250) and transmission electron spectroscopy (TEM; JEOL JEM-1400). The specific surface area and pore size distribution of materials were obtained with a Brunauer–Emmett–Teller (BET) analyzer (Micromeritics Instrument Corporation TriStar II 3020). The BET test using nitrogen adsorption/desorption isotherms was performed at −196 °C, and pore size distribution was calculated by means of the Kruk–Jaroniec–Sayari (KJS) method.

Electrochemical measurements

Rotating disk electrode (RDE) and rotating ring-disk electrode (RRDE) techniques controlled by AUTOLAB 760E (CH Instruments) workstation with a rotation source of research instrumentation (Pine Research, USA) were used to evaluate the electrochemical performance of the electrocatalysts. A standard three-electrode system was employed to test the ORR performance, consisting of a carbon rod as counter-electrode, a saturated calomel electrode (SCE) as reference electrode, and an electrocatalyst-coated glass carbon electrode (GCE; surface area 0.19625 cm^2) as working electrode. All potentials in this work were calibrated with reference to the RHE. The measured potentials *vs.* SCE were converted to the RHE scale according to the Nernst equation (1), where $E_{Hg/HgCl}$ is the experimentally measured potential *vs.* Hg/HgCl reference and $E^{\circ}_{Hg/HgCl} = 0.244$ V at 25 °C.

$$E_{RHE} = E_{Hg/HgCl} + 0.059\,pH + E^{\circ}_{Hg/HgCl} \quad (1)$$

The working electrode of the as-prepared electrocatalyst was made as follows. Five milligrams of electrocatalyst was added into a solution including 750 μL deionized water and 200 μL isopropyl alcohol with Nafion solution (50 μL) and ultrasonically dispersed for 30 min to obtain a homogeneous slurry. Then, 10 μL of the slurry was uniformly dropped onto a freshly polished GDE with a loading of 0.24 mg_{cat} cm^{-2} and dried under ambient conditions. For comparison, the Pt/C catalyst (20 wt% Pt/C) was prepared in the same way using the same amount of catalyst.

The transferred electron number for the ORR was estimated by the Koutecký–Levich (K–L) equation (2) and (3)

$$1/J = 1/J_K + 1/J_L \quad (2)$$

$$B\omega^{1/2} = 0.62nFC_o\omega^{1/2}D_o^{2/3}\nu^{1/6} \quad (3)$$

where J is the measured current density, J_K is the kinetic current density, J_L is the diffusion-limited current density, ω is the electrode rotation rate, F is the Faraday constant (96 485 C mol^{-1}), C_o is the bulk concentration of O_2 (1.2×10^{-6} mol cm^{-3} for 0.1 M KOH solution), D_o is the diffusion coefficient of O_2 (1.9×10^{-5} cm^2 s^{-1} for 0.1 M KOH solution); and ν is the kinetic viscosity of the electrolyte (0.01 cm^2 s^{-1} for 0.1 M KOH solution).

The ORR is an electron charge transfer reaction with two main possible paths:[4] one is a one-step direct pathway, involving O_2 acquiring four electrons to produce OH^- directly, as shown in eqn (4); the other is a two-step indirect pathway,

involving two-electron transfer to produce HO_2^- in the first step followed by HO_2^- getting another two electrons to transform it into OH^- in the second step, as shown in eqn (5) and (6), and it should be added that HO_2^- will be transformed into H_2O_2.

$$O_2 + 2H_2O + 4e^- \rightarrow 4OH^- \quad (4)$$

$$O_2 + H_2O + 2e^- \rightarrow HO_2^- + OH^- \quad (5)$$

$$HO_2^- + H_2O + 2e^- \rightarrow 3OH^- \quad (6)$$

For the RRDE measurement, the disk electrode was scanned at a rate of 10 mV s^{-1} and the ring potential was set constant at 0.8 V. The H_2O_2% (the content of H_2O_2 generated) and n (the number of electrons transferred) were determined by the followed equations:

$$y = 200I_R/(NI_d + I_r) \quad (7)$$

$$n = 4NI_R/(NI_D + I_R) \quad (8)$$

where I_d is disk current, I_r is ring current, and N is current collection efficiency of the Pt ring ($N = 0.394$).

Results and discussion

The preparation process of PFCMs is illustrated in Fig. 1 and the detailed method can be found in the Experimental section. Fig. 2A presents the X-ray diffraction (XRD) pattern of CPDCFs, with a broad peak at 25° corresponding to amorphous carbon. This peak becomes sharp and shifts positively to 26° in XRD patterns of PFCMs, ascribed to the (002) facet of graphitic carbon. In addition, part of the peaks located at about 30.01 and 43.43 is indexed to the (101) and (111) planes, respectively, of the Fe_3N phase (JCPDS no. 49-1664), and the obvious peak at about 31.65 is attributed to Fe_2N (JCPDS no. 50-0957), and the remaining peak is FeN (JCPDS no. 50-1087). The XRD patterns demonstrate the existence of Fe–N species in the PFCMs.[19]

The degree of graphitization was confirmed by Raman spectroscopy.[20,21] All Raman lines obtained were treated with a linear baseline subtraction and then deconvoluted to Lorentzian lines. The D band can be ascribed to defects or sp^3 C, whereas the G band is the characteristic peak of graphitic carbon.[22] As shown in Fig. 2B, all the samples displayed typical G and D bands, the former of which is assigned to the E_{2g} mode of sp^2 carbon atoms and the distorted carbon frames on the defect sites (I_D/I_G values for samples are shown in Table S1†). The increasing ratio of I_D/I_G (2.30 to 2.77) indicates that the defects of the graphite structure grow along with the increment of annealing temperature.[23] Based on the above results, it is inconclusive whether the annealing treatment leads to the increment of the graphitization degree as well as the defects, which is highly desirable for an advanced catalyst.

X-ray photoelectron spectroscopy (XPS) was also used for the investigation of elemental composition and binding configurations of N and Fe atoms.[24–30] The XPS survey spectra of CPDCFs and PFCMs-1000 confirm the presence of Fe and N elements (Fig. 2C). Table S2† presents the surface elemental content for both catalysts. As shown in Fig. 2D, the Fe $2p_{3/2}$ spectrum shows multiple peaks, which indicates that the metal species are complicated in terms of their chemical state. According to previous reports, the Fe $2p_{3/2}$ peak located at around 712 eV is due to N-coordinated iron.[25,26] This metal species has been demonstrated to be mainly responsible for active centers on iron- and nitrogen-codoped carbon materials. The other peaks may be attributed to Fe^{2+} (709.05 eV) and Fe^{3+} (710.8 eV), and the corresponding satellite peaks (714.3 and 716.1 eV respectively).[27,28] The N 1s XPS spectra of CPDCFs and PFCMs-1000 are deconvoluted into four peaks in Fig. 2E. Two peaks located at 400.5 and 401.2 eV are observed in CPDCFs, confirming the existence of pyrrolic N and graphitic N, while for PFCMs-1000, a new peak located at about 398.6 eV appears, demonstrating the formation of pyridinic N.[29,30] The comparison of XPS spectra between CPDCFs and PFCMs-1000

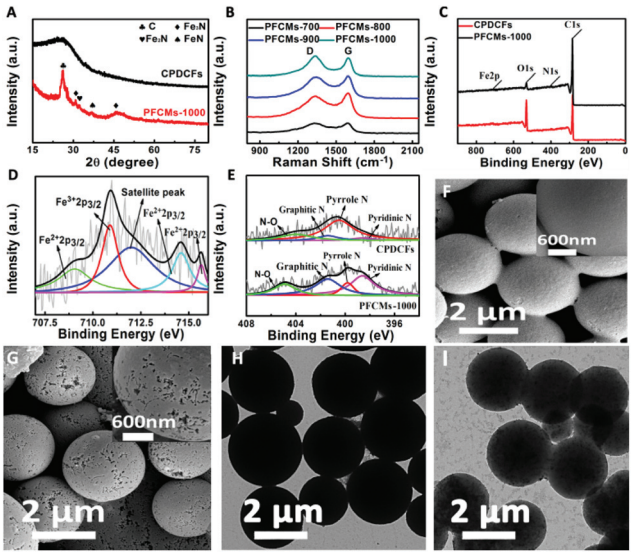

Fig. 2 (A) XRD patterns of the CPDCFs and PFCMs-1000. (B) Raman spectra of PFCMs with different annealing temperatures. (C) XPS survey spectra for CPDCFs and PFCMs-1000. (D) XPS spectrum of PFCMs-1000 in the Fe 2p region. (E) High-resolution N 1s scans of CPDCFs and PFCMs-1000. FESEM images for (F) CPDCFs and (G) PFCMs-1000. TEM images for (H) CPDCFs and (I) PFCMs-1000.

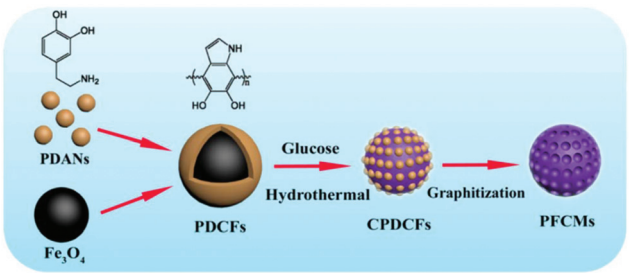

Fig. 1 Illustration of synthetic process of PFCMs.

illustrates the high-temperature treatment leads to a change in N type, with the content of pyridinic N rising. Considering the vital role of pyridinic N for ORR,[31,32] PFCMs-1000 has great potential as an advanced catalyst for oxygen reduction.

The morphology of catalysts was further investigated by field emission scanning electron microscopy (FESEM) and transmission electron microscopy (TEM). The SEM image of the precursor shows well-defined nanosphere morphology (Fig. S1†). As shown in Fig. 2F, CPDCFs have smooth surface and regular sphere morphology. Fig. 2G shows that PFCMs-1000 contains porous structures and the average pore diameter is approximately 70 nm (Fig. S2†). The energy dispersive X-ray (EDX) spectrum reveals the atomic ratio of C, N, O and Fe elements (Fig. S3†). TEM images of PFCMs-1000 show interconnected porous architecture (Fig. 2I). The generation of porous structure is beneficial for the rate of electrolyte access and ion diffusion, and is highly desirable for an advanced catalyst. The pore structures of CPDCFs and PFCMs-1000 were investigated by the N_2 adsorption–desorption isotherms. PFCMs-1000 exhibit distinct capillary condensation steps (Fig. S4B†), which is indicative of the presence of porous structure for the sample. The BET surface areas of CPDCFs and PFCMs-1000 are found to be 17.6 and 760.4 $m^2\ g^{-1}$. Moreover, the average pore sizes of the two samples are calculated at about 5.9 and 3.4 nm. The above results clearly demonstrated that high-temperature annealing plays a vital role in the surface area increment, which is one of the necessary factors for an advanced catalyst.

To evaluate the electrocatalytic ORR performance, PFCMs was deposited on a glass carbon electrode and tested using an aqueous-based electrochemical setup at ambient conditions. All potentials are reported on the RHE scale. The ORR activities of PFCMs were first evaluated by cyclic voltammetry (CV) in O_2- and N_2-saturated 0.1 M KOH solution. They all exhibited well-defined reduction peaks in O_2-saturated electrolyte while no obvious cathodic peaks were found in N_2-saturated electrolyte (Fig. 3A). We measured the electrical double-layer capacitance (EDLC) by CV as an indication of electrochemically active surface area, as depicted in Fig. 3B. From the CV results, it is concluded that the EDLC of PFCMS has been greatly increased with the rise of calcination temperature (from 4.86 to 167.91 F g^{-1}).[33]

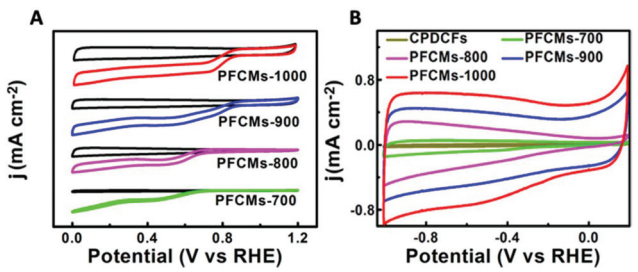

Fig. 3 (A) Cyclic voltammograms of four PFCMs samples in O_2-saturated and N_2-saturated (black lines) electrolyte. (B) Cyclic voltammetry in N_2-saturated 0.1 M NaOH.

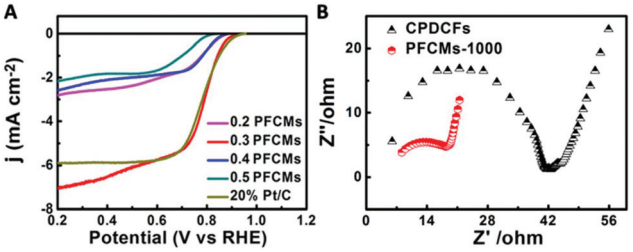

Fig. 4 (A) The RDE polarization curves of PFCMs-1000 synthesized using different glucose concentrations and commercial Pt/C. (B) EIS plots of the PFCMs-1000- and CPDCFs-based electrodes.

The improved ORR activity of PFCMs-1000 compared with CPDCFs seems to be related to enlarged exposure of N–C sites and Fe-related ORR active sites with a higher specific ORR activity.[34] We chose the glucose concentration used in synthesis as a control condition to evaluate the performance of catalysts. In Fig. 4A, we can see that the onset potential increases with the increment of glucose concentration from 0.2 M to 0.3 M, but further increment of the concentration causes decreasing onset potential. This could be due to the fact that with the addition of glucose, the conductivity of the cathode increases, thus promoting electron transfer in the reaction process. However, beyond the optimum concentration, high electroconductibility does not help in performance, and so oxygen reduction rate decreases and fewer ions are produced due to the blockage of active sites by electrolyte and the decrease of active sites.[35] Then, rotating disk electrode (RDE) measurements were performed for PFCMs (fabricated with a glucose concentration of 0.3 M) annealed at various temperature from 700–1000 °C. As shown in Fig. S5,† PFCMs-1000 shows the best ORR performance among the as-prepared materials, even better than the commercial Pt/C (20 wt%) catalyst. The onset potential of PFCMs-1000 was more positive than that of CPDCFs, indicating that annealing treatment increases the electrochemical activity of ORR. A more detailed comparison is given in Table S3.† Electrochemical impedance spectroscopy (EIS) was performed in the frequency range from 0.1 Hz to 10^6 Hz. As shown in Fig. 4B, the Nyquist plots of the electrodes with different catalysts represent a well-defined frequency-dependent semicircular impedance curve. The semicircle diameter in the EIS of PFCMs-1000 is much lower than for CPDCFs, illustrating the smaller impedance in PFCMs-1000.[36–38] This might be due to increase in degree of graphitization, which results in enhanced conductivity, thus promoting electron transfer in the reaction process.

The ORR kinetic processes were evaluated by using linear sweep voltammetry (LSV) at different rotation speeds with a scan rate of 5 mV s^{-1}. Fig. 5A shows the diffusion current densities depended on the rotation rates, suggesting that the ORR behaviour of PFCMs-1000 is dominated by a diffusion-controlled process. The corresponding Koutecký–Levich (K–L) (equation (2) and (3)) plots exhibited good linearity over the potential range from 0.5 to 0.7 V (Fig. 5B), with a slope more

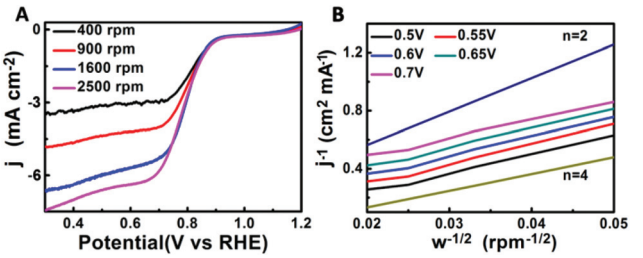

Fig. 5 (A) LSV curves at various rotation speeds. (B) The corresponding K–L plots at different potentials.

similar to that of an ideal four-electron process than to an ideal two-electron process. Especially, the number of electrons calculated is 3.8 at 0.6 V. A more in-depth RRDE study of the electron transport pathway was undertaken based on the assumption of a four-electron system.

To verify the ORR catalytic pathways of the PFCMs-1000, we performed rotating ring-disk electrode (RRDE) measurements to monitor the formation of peroxide species (HO_2^-) during the ORR process (Fig. 6A).[39] The measured HO_2^- yields are below ~10%, over the potential range of 0.4–0.8 V, giving an electron transfer number of ~3 : 9 (Fig. 6B). This is consistent with the result obtained from the K–L plots based on RDE measurements, suggesting the ORR catalysed by PFCMs-1000 is mainly by four-electron reduction.

Stability is another critical parameter to evaluate the performance of catalysts. Besides high activity, PFCMs-1000 also exhibited respectable catalytic stability in 0.1 M KOH. As shown in Fig. 7A, PFCMs-1000 retains 96% of the initial current density after 10 000 s chronoamperometric testing, which was better than that of the commercial Pt/C catalyst (with a decrease of 27%) in the same condition. As shown in Fig. S6,† the TEM image of PFCMs-1000 after long-term stability testing shows almost no obvious change in morphology. Furthermore, as the methanol crossover effect of the catalysts is also an important factor for practical application, the methanol-tolerance of the PFCMs-1000 and the commercial Pt/C in 0.1 M KOH electrolyte was compared.[40] It can be seen from Fig. 7B that after the addition of 1 M methanol to the electrolyte, no significant change was observed in the ORR current at

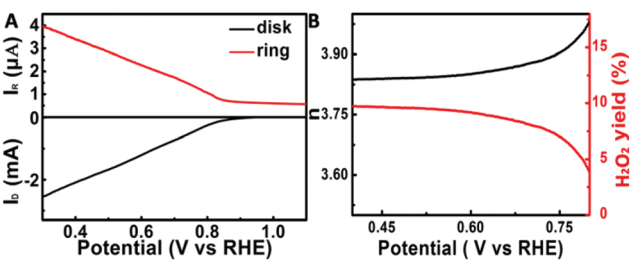

Fig. 6 (A) RRDE curves of PFCMs-1000 in O_2-saturated 0.1 M KOH. (B) Percentage of peroxide (red line) and the electron transfer number (*n*) (black line) of PFCMs-1000 at various potentials based on the corresponding RRDE data.

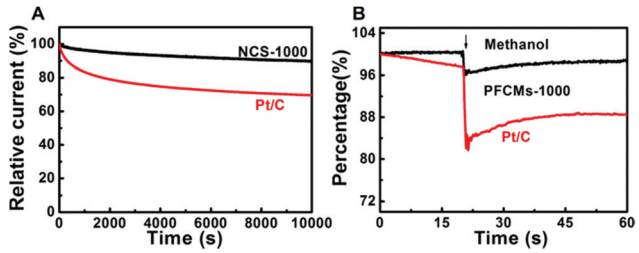

Fig. 7 (A) Comparison of the chronoamperometric response of PFCMs-1000 and Pt/C over 4000 s at 0.8 V with a constant rotation speed of 1600 rpm in O_2-saturated solution of 0.1 M KOH. The arrow in (B) represents the addition of 1 M methanol into the electrolyte.

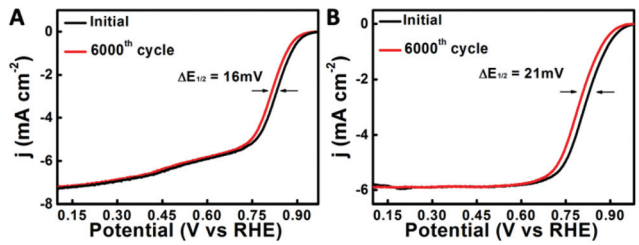

Fig. 8 RDE polarization curves of (A) PFCMs catalyst and (B) Pt/C before and after 6000 potential cycles in O_2-saturated 0.1 M KOH, respectively. Potential cycling was carried out between 0 and 1.2 V *versus* RHE at 50 mV s^{-1}.

PFCMs-1000. In contrast, the ORR current for the Pt/C catalyst decreased sharply. These results indicate that the PFCMs-1000 catalyst has better stability and resistance to methanol crossover for ORR than the commercial Pt/C catalyst.

The durability is a key factor in electrocatalysis.[41–46] The PFCMs-1000 catalyst was also tested by cycling the catalysts between 0 and 1.2 V at 50 mV s^{-1} under O_2 atmosphere. After 6000 continuous cycles, the half-wave potential $E_{1/2}$ exhibited a small negative shift of 16 mV under O_2 cycling (Fig. 8A), which is comparable to the Pt/C catalyst (21 mV negative shift, Fig. 8B) and most non-precious metal catalysts,[5,11] indicating the high stability of PFCMs.

Conclusions

In this study, PFCMs porous spheres have been successfully proven as an efficient and selective catalyst for electrochemical reduction of O_2 in alkaline media under ambient conditions. PFCMs electrocatalysts exhibit large surface area of 760.3 m^2 g^{-1} and porous structure as determined by nitrogen sorption isotherms. The structural uniqueness, such as porous structure and high surface area, provides more accessibility to the catalytically active sites. The ORR catalytic performance of PFMCs electrocatalysts approaches that of commercial Pt/C catalyst in basic media, exhibiting similar half-wave potential (0.836 V) and onset potential (0.949 V) but higher kinetic

current density (6.21 mA cm^{-2}). Furthermore, in contrast to Pt/C, the PFCMs electrocatalysts show higher resistance to poisoning by methanol and better durability. This work not only provides us an attractive Earth-abundant catalyst material for the ORR, but also opens up an exciting new avenue to the rational design of porous nanostructures as advanced electrocatalysts.

Conflicts of interest

There are no conflicts to declare.

Acknowledgements

This work was supported by the National Key Scientific Instrument and Equipment Development Project of China (No. 21627809), the National Natural Science Foundation of China (No. 21601064) and the Special Foundation for Taishan Scholar Professorship of Shandong Province (No. ts20130937).

References

1 M. Liu, R. Zhang and W. Chen, *Chem. Rev.*, 2014, **114**, 5117–5160.
2 C. Jiang, J. Ma, G. Corre, S. L. Jain and J. T. S. Irvine, *Chem. Soc. Rev.*, 2017, **46**, 2889–2912.
3 H. Zhang, H. Osgood, X. Xie, Y. Shao and G. Wu, *Nano Energy*, 2017, **31**, 331–350.
4 Z. Tang, W. Wu and K. Wang, *Catalysts*, 2018, **8**, 65.
5 G. Wu, K. L. More, C. M. Johnston and P. Zelenay, *Science*, 2011, **332**, 443–447.
6 M. K. Debe, *Nature*, 2012, **486**, 43–51.
7 U. I. Kramm, I. Herrmann-Geppert, J. Behrends, K. Lips, S. Fiechter and P. Bogdanoff, *J. Am. Chem. Soc.*, 2016, **138**, 635–640.
8 K. Strickland, E. Miner, Q. Jia, U. Tylus, N. Ramaswamy, W. Liang, M.-T. Sougrati, F. Jaouen and S. Mukerjee, *Nat. Commun.*, 2015, **6**, 7343.
9 J. Liang, R. F. Zhou, X. M. Chen, Y. H. Tang and S. Z. Qiao, *Adv. Mater.*, 2014, **26**, 6074–6079.
10 D. Deng, L. Yu, X. Chen, G. Wang, L. Jin, X. Pan, J. Deng, G. Sun and X. Bao, *Angew. Chem., Int. Ed.*, 2013, **52**, 371–375.
11 H. Yang, J. O. Jensen, W. Zhang, L. N. Cleemann, W. Xing, N. J. Bjerrum and Q. Li, *Angew. Chem., Int. Ed.*, 2014, **53**, 3675–3679.
12 A. Zitolo, V. Goellner, V. Armel, M.-T. Sougrati, T. Mineva, L. Stievano, E. Fonda and F. Jaouen, *Nat. Mater.*, 2015, **14**, 937–942.
13 Y. Zheng, Y. Jiao, M. Jaroniec, Y. Jin and S. Z. Qiao, *Small*, 2012, **8**, 3550–3566.
14 D.-W. Wang and D. Su, *Energy Environ. Sci.*, 2014, **7**, 576–591.
15 Y. J. Sa, C. Park, H. Y. Jeong, S.-H. Park, Z. Lee, K. T. Kim, G.-G. Park and S. H. Joo, *Angew. Chem., Int. Ed.*, 2014, **53**, 4102–4106.
16 J. Masa, W. Xia, I. Sinev, A. Zhao, Z. Sun, S. Grutzke, P. Weide, M. Muhler and W. Schuhmann, *Angew. Chem., Int. Ed.*, 2014, **53**, 8508–8512.
17 Z.-S. Wu, S. Yang, Y. Sun, K. Parvez, X. Feng and K. Müllen, *J. Am. Chem. Soc.*, 2012, **134**, 9082–9085.
18 W. Qiang, W. Li, X. Li, X. Chen and D. Xu, *Chem. Sci.*, 2014, **5**, 3018–3024.
19 T. Sun, M. Yang, H. Chen, Y. Liu and H. Li, *Appl. Catal., A*, 2018, **559**, 102–111.
20 J. Zhang, Z. Zhao, Z. Xia and L. Dai, *Nat. Nanotechnol.*, 2015, **10**, 444–452.
21 Z. R. Ismagilov, A. E. Shalagina, O. Y. Podyacheva, A. V. Ischenko, L. S. Kibis, A. I. Boronin, Y. A. Chesalov, D. I. Kochubey, A. I. Romanenko and O. B. Anikeeva, *Carbon*, 2009, **47**, 1922–1929.
22 Y. Liu, Y. Su, X. Quan, X. Fan, S. Chen, H. Yu, H. Zhao, Y. Zhang and J. Zhao, *ACS Catal.*, 2018, **8**, 1186–1191.
23 O. A. Maslova, M. R. Ammar, G. Guimbretière, J. N. Rouzaud and P. Simon, *Phys. Rev. B: Solid State*, 2012, **86**, 134205.
24 P. Chen, L.-K. Wang, G. Wang, M.-R. Gao, J. Ge, W.-J. Yuan, Y.-H. Shen, A.-J. Xie and S.-H. Yu, *Energy Environ. Sci.*, 2014, **7**, 4095–4103.
25 M. Zhou, C. Yang and K. Y. Chan, *Adv. Energy Mater.*, 2014, **4**, 1400840.
26 H. Zhong, C. Deng, Y. Qiu, L. Yao and H. Zhang, *J. Mater. Chem. A*, 2014, **2**, 17047–17057.
27 D. Yu, Q. Zhang and L. Dai, *J. Am. Chem. Soc.*, 2010, **132**, 15127–15129.
28 K. Parvez, S. Yang, Y. Hernandez, A. Winter, A. Turchanin, X. Feng and K. Müllen, *ACS Nano*, 2012, **6**, 9541–9550.
29 M. Vikkisk, I. Kruusenberg, U. Joost, E. Shulga and K. Tammeveski, *Electrochim. Acta*, 2013, **87**, 709–716.
30 Y. Jia, L. Zhang, A. Du, G. Gao, J. Chen, X. Yan, C. L. Brown and X. Yao, *Adv. Mater.*, 2016, **28**, 9532–9538.
31 Q. Niu, J. Guo, Y. Tang, X. Guo, J. Nie and G. Ma, *Electrochim. Acta*, 2017, **255**, 72–82.
32 X. Cui, S. Yang, X. Yan, J. Leng, S. Shuang, P. M. Ajayan and Z. Zhang, *Adv. Funct. Mater.*, 2016, **26**, 5708–5717.
33 C. Kim, K.-S. Yang and W.-J. Lee, *Electrochem. Solid. State Lett.*, 2004, **7**, A397–A399.
34 B. Jeong, D. Shin, M. Choun, S. Maurya, J. Baik, B. S. Mun, S.-H. Moon, D. Su and J. Lee, *J. Phys. Chem. C*, 2016, **120**, 7705–7714.
35 M. M. Hossen, K. Artyushkova, P. Atanassov and A. Serov, *J. Power Sources*, 2018, **375**, 214–221.
36 T. Meng, L. Zheng, J. Qin, D. Zhao and M. Cao, *J. Mater. Chem. A*, 2017, **5**, 20228–20238.
37 X. Li, Y. Fang, X. Lin, M. Tian, X. An, Y. Fu, R. Li, J. Jin and J. Ma, *J. Mater. Chem. A*, 2015, **3**, 17392–17402.

38 Z. Jin, H. Nie, Z. Yang, J. Zhang, Z. Liu, X. Xu and S. Huang, *Nanoscale*, 2012, **4**, 6455–6460.
39 W. Yang, X. Liu, X. Yue, J. Jia and S. Guo, *J. Am. Chem. Soc.*, 2015, **137**, 1436–1439.
40 L. Carrette, K. A. Friedrich and U. Stimming, *ChemPhysChem*, 2000, **1**, 162–193.
41 X. Ren, R. Ge, Y. Zhang, D. Liu, D. Wu, X. Sun, B. Du and Q. Wei, *J. Mater. Chem. A*, 2017, **5**, 7291–7294.
42 X. Ren, W. Wang, R. Ge, S. Hao, F. Qu, G. Du, A. M. Asiri, Q. Wei, L. Chen and X. Sun, *Chem. Commun.*, 2017, **53**, 9000–9003.
43 X. Ren, D. Wu, R. Ge, X. Sun, H. Ma, T. Yan, Y. Zhang, B. Du, Q. Wei and L. Chen, *Nano Res.*, 2018, **11**, 2024–2033.
44 D. Wu, Y. Wei, X. Ren, X. Ji, Y. Liu, X. Guo, L. Liu, A. M. Asiri, Q. Wei and X. Sun, *Adv. Mater.*, 2018, **30**, 1705366–1705372.
45 X. Ren, X. Ji, Y. Wei, D. Wu, Y. Zhang, M. Ma, Z. Liu, A. M. Asiri, Q. Wei and X. Sun, *Chem. Commun.*, 2018, **54**, 1425–1428.
46 X. Ren, G. Cui, L. Chen, F. Xie, Q. Wei, Z. Tian and X. Sun, *Chem. Commun.*, 2018, **54**, 8474–8477.